Internal Tides and Turbulence along the 3000-m Isobath of the Hawaiian Ridge

CRAIG M. LEE,* ERIC KUNZE,+ THOMAS B. SANFORD,* JONATHAN D. NASH,# MARK A. MERRIFIELD,@ AND PETER E. HOLLOWAY&,**

*Applied Physics Laboratory, University of Washington, Seattle, Washington
+School of Earth and Ocean Sciences, University of Victoria, Victoria, British Columbia, Canada
#College of Oceanic and Atmospheric Sciences, Oregon State University, Corvallis, Oregon
@School of Ocean and Earth Science Technology, University of Hawaii, Honolulu, Hawaii
&School of Geography and Oceanography, Australian Defence Force Academy, University of New South Wales, Canberra, New South Wales, Australia

(Manuscript received 20 October 2004, in final form 4 October 2005)

ABSTRACT

Full-depth velocity and density profiles taken along the 3000-m isobath characterize the semidiurnal internal tide and bottom-intensified turbulence along the Hawaiian Ridge. Observations reveal baroclinic energy fluxes of 21 ± 5 kW m^{-1} radiating from French Frigate Shoals, 17 ± 2.5 kW m^{-1} from Kauai Channel west of Oahu, and 13 ± 3.5 kW m^{-1} from west of Nihoa Island. Weaker fluxes of 1–4 ± 2 kW m^{-1} radiate from the region near Necker Island and east of Nihoa Island. Observed off-ridge energy fluxes generally agree to within a factor of 2 with those produced by a tidally forced numerical model. Average turbulent diapycnal diffusivity K is (0.5–1) × 10^{-4} m^2 s^{-1} above 2000 m, increasing exponentially to 20 × 10^{-4} m^2 s^{-1} near the bottom. Microstructure values agree well with those inferred from a finescale internal wave-based parameterization. A linear relationship between the vertically integrated energy flux and vertically integrated turbulent dissipation rate implies that dissipative length scales for the radiating internal tide exceed 1000 km.

1. Introduction

Recent findings that significant surface tide losses occur at abrupt deep-ocean topography have rejuvenated interest in internal tides. Assimilation of satellite altimetry into the barotropic tidal equations suggests that up to one-third of the surface tide loss (0.8 TW) occurs at deep-ocean ridges, trenches, and island chains (Egbert and Ray 2001) in contrast to past assumptions that most tidal dissipation occurs in shallow shelves and seas (Jeffries 1920; Wunsch 1975). Using a two-layer global model, Simmons et al. (2004, hereinafter SHA) find that features covering 10% of the seafloor account for 75% of the predicted surface tide loss. Conversion occurs most efficiently for strong tidal flows that cross topography (Baines 1982). Thus, open-ocean sites produce larger losses than those associated with shelves and shelf breaks where tidal currents tend to flow parallel to shelf/slope topography (Sjöberg and Stigebrandt 1992). Were the energy associated with these losses turbulently dissipated in the abyss, it would provide approximately one-half of the deep mixing required to close the meridional thermohaline circulation (Munk and Wunsch 1998). The possibility that surface tide conversion and eventual dissipation contributes a significant fraction of the "missing" abyssal mixing motivates efforts to understand the conversion from barotropic to baroclinic (internal) tide, including the partitioning between local dissipation and internal tide radiation.

Satellite altimetry also reveals coherent, low-mode internal tides radiating thousands of kilometers from suspected generation sites at prominent midocean topographic features (Ray and Mitchum 1997; Kantha and Tierney 1997; Cummins et al. 2001; Dushaw 2002). In situ observations (Althaus et al. 2003) show that only 1% of the energy lost from the surface tide at the Mendocino Escarpment dissipates locally with the bulk radiating away as internal waves. These results suggest that radiating internal tides could provide significant

** Deceased.

Corresponding author address: Craig M. Lee, Applied Physics Laboratory, 1013 NE 40th St., Seattle, WA 98105-6698.
E-mail: craig@apl.washington.edu

energy for mixing well away from their generation sites, and not necessarily in abyssal waters.

Motivated by the potentially important contribution of tidal conversion to global mixing, the multi-investigator Hawaii Ocean Mixing Experiment (HOME) observational program focused on understanding surface tide losses, internal tide generation, turbulent dissipation/mixing, and internal wave radiation associated with tide–topography interactions along the Hawaiian Ridge. Previous studies of global surface tide based on remotely sensed sea surface height (e.g., Egbert and Ray 2001) found the Hawaiian Ridge to be a region of particularly intense loss per unit surface area. Initial HOME efforts concentrated on historical analysis (Finnigan et al. 2002; Lukas et al. 2001) and modeling (Holloway and Merrifield 1999; Kang et al. 2000; Merrifield et al. 2001; Merrifield and Holloway 2002; Johnston and Merrifield 2004; Johnston et al. 2003). Results from these studies guided the design of three intensive measurement programs: Survey (Rudnick et al. 2003; Martin et al. 2006; Nash et al. 2006; Klymak et al. 2006), Farfield (Dushaw 2003; Rainville and Pinkel 2006), and Nearfield (Kunze et al. 2003; Carter and Gregg 2003; Avicola et al. 2003). This paper presents results from the Survey component, which conducted a broad census of internal tide variability along the Hawaiian Ridge. Because Survey sampling intentionally included both low- and high-energy environments, these measurements provide a means to evaluate and refine numerical investigations and assimilations of satellite altimetry. Survey program results subsequently guided site choice for the intensive Nearfield measurement effort.

This paper utilizes full-depth profile time series taken along the 3000-m isobath of the Hawaiian Ridge to quantify semidiurnal horizontal velocities, isopycnal displacements, energies, energy fluxes, and turbulent dissipation rates. Primary goals include (i) identification of regions of energetic internal tide and (ii) evaluation of numerical- and altimetry-based results. We begin by detailing the measurement program and the data collected by the absolute velocity profiler (AVP) and CTD. The next section summarizes analysis techniques, followed by a comparison of observations with results from numerical simulations (Merrifield et al. 2001; Merrifield and Holloway 2002; Holloway and Merrifield 2003). Nash et al. (2006) employ an intensive expendable current profiler (XCP)/AVP survey collected on the same cruise to describe the structure of the semidiurnal internal wave field across the south side of Kaena Ridge from the ridge crest (~1000-m isobath) to the 3000-m isobath.

2. Data

As part of the Survey program (Pinkel et al. 2000; Rudnick et al. 2003), profile time series taken at 14 sites (Fig. 1) characterize along-ridge semidiurnal tide variability from Kauai Channel (west of Oahu) to French Frigate Shoals (950 km north-northwest). With the aid of numerical simulations (Merrifield et al. 2001), sites were selected to represent areas of strong (Kauai Channel, Nihoa Island, French French Frigate Shoals) and weak (Necker Island) internal tide energy flux on both sides of the ridge crest. Sampling during spring tides focused on regions predicted to have large energy flux (Fig. 2). Numerical simulations (Merrifield and Holloway 2002) and finescale surveys (Nash et al. 2006) suggest that the strongest internal tide generation occurs along the ridge crest rim between the 1000- and 1500-m isobaths, forming beams that reflect from the surface and bottom beyond the 4000-m isobath. Thus, the selected locations along the 3000-m isobath sample the fully developed, radiating internal tide after it departs from the ridge but before it can form standing modes. The 19-day measurement program (10–29 October 2000) spanned two spring tides and the intervening neap (Fig. 2). The factor-of-2 difference between spring and neap velocity (factor of 4 in energy) motivated repeat occupations of two stations south of the ridge crest at French Frigate Shoals (06 and 06a) and two off Nihoa Island (04 and 04a) to investigate spring–neap variability in the internal wave field.

The free-falling AVP (Sanford et al. 1985) collected 78 full-depth (surface to 1 m above the seafloor) profiles of finescale horizontal velocity (u, v), temperature T, salinity S, optical backscatter, and microscale shear (u_z, v_z). At each site, four to six full-depth profile pairs (down- and upcasts) executed over 10–15 hours allow extraction of semidiurnal from other internal wave frequencies. Additional profiles using XCPs and a CTD extended the length of the AVP time series to provide enhanced ability to isolate the semidiurnal signal. The Research Vessel (R/V) *Wecoma*'s Sea-Bird 911+ CTD system provided full-depth profiles of temperature and salinity, while the XCPs measured velocity and temperature in the upper 1600–2000 m.

The AVP measures horizontal velocity (u, v) relative to an unknown but depth-independent constant (Sanford et al. 1985). These velocities are made absolute by matching them with GPS-referenced shipboard ADCP profiles in the 60–140-m depth range. ADCP velocities were made absolute using single-ping ADCP profiles corrected for the ship's velocity with GPS heading and differential GPS (DGPS) position information. The correction employed average ADCP profiles within

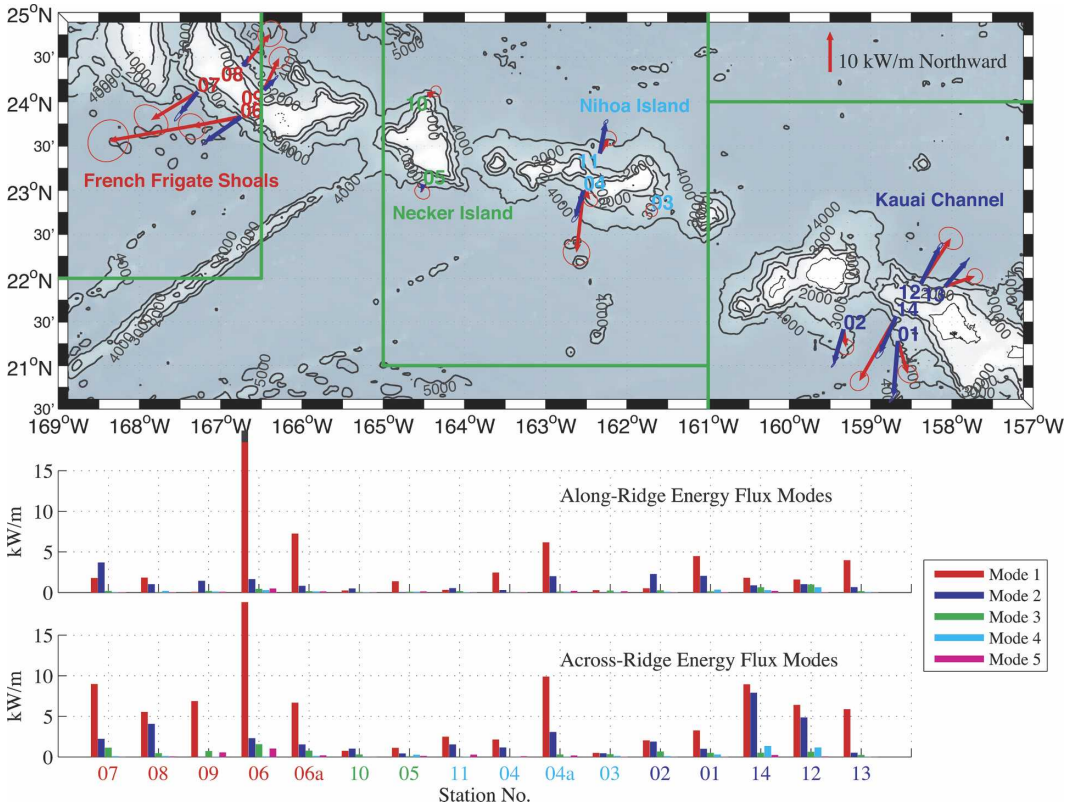

FIG. 1. (top) AVP (red) and model (blue) depth-integrated energy-flux vectors with numbers marking station locations. Small red (blue) ellipses mark observed (modeled) energy flux standard errors. Green boxes delimit model domains. (bottom) Modal decomposition of AVP (middle) along-ridge and (bottom) across-ridge energy fluxes at each station. Across-ridge fluxes are larger at most sites, with the notable exception of station 06. Mode 1 dominates cross-ridge fluxes, though mode 2 is comparable at stations 8, 12, and 14. Mode 1 also dominates most along-ridge fluxes, though mode 2 is larger at stations 7 and 9.

±500 s of AVP sinking (or the ship coming alongside AVP); data when the ship was turning more rapidly than 0.2° s^{-1} were excluded. Velocity uncertainties are ±1 cm s^{-1}. Sea-Bird sensors measured temperature, salinity, and pressure with quoted uncertainties of ±0.001°C, ±0.002 ppt, and ±0.1 dbar, resulting in density uncertainties of 0.002 kg m^{-3}. Two microscale shear probes were used to estimate the turbulent kinetic energy dissipation rate ε. Processing details for the microscale measurements can be found in the appendix. Klymak et al. (2006) use these microstructure data in a more complete assessment of turbulent mixing in the vicinity of the Hawaiian Ridge, developing a cross-ridge/depth structure turbulence function based on all available microstructure measurements.

3. Analysis

Time series of full-depth AVP and CTD profiles provide estimates of semidiurnal fluctuations of horizontal velocity $[\hat{u}(z, t), \hat{v}(z, t)]$, vertical velocity $\hat{w}(z, t)$, vertical displacement $\hat{\xi}(z, t)$, and baroclinic reduced pressure anomaly $\hat{p}(z, t)$. Calculations employing horizontal velocity data from AVP up- and downcasts use 8–12 velocity profiles per station. Because AVP temperature and conductivity sensors protrude from the profiler's base, upcast data exhibit contamination from entrained water. Therefore, potential density time series use only AVP and CTD downcasts, providing 4–11 profiles per site. Perturbation velocities $[u'(z, t), \hat{v}(z, t)]$ were calculated as

$$u'(z,t) = u(z,t) - \langle u(z,t)\rangle_t - \frac{1}{H}\int_{-H}^{0} [u(z,t) - \langle u(z,t)\rangle_t]\, dz,$$

where H is profile depth, $\langle\rangle_t$ indicates time averaging over a station occupation, and the last term on the right-hand side ensures that perturbation velocities satisfy the baroclinicity condition of zero depth-average flow. The offset of isopycnals from their time-averaged (over at least one semidiurnal cycle) depths defines perturbation vertical displacement $\xi'(z, t)$ (Desaubies and Gregg 1981). Perturbation potential density, $\rho'_\theta(z, t) =$

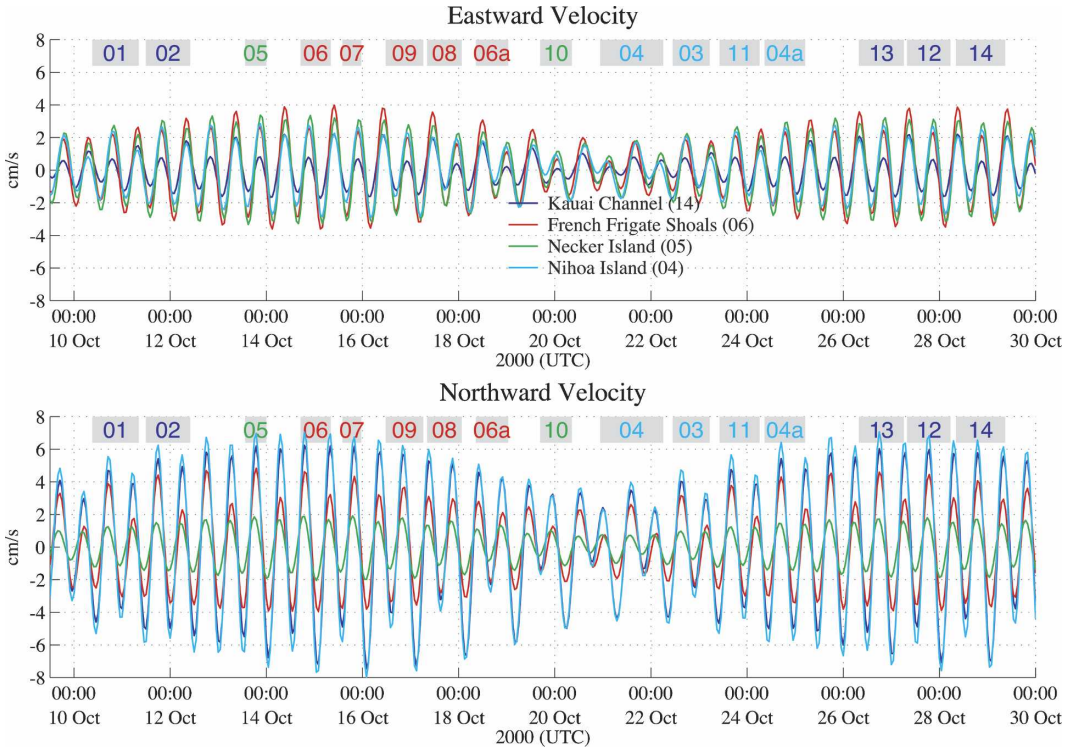

FIG. 2. (top) East and (bottom) north surface tide velocities during the AVP sampling interval. Numbers and gray bars (duration) running across the top of each panel mark AVP station occupations. Time series and station numbers are color coded by location (Kauai Channel: navy blue, French Frigate Shoals: red, Necker Island: green, and Nihoa Island: light blue).

$\rho_\theta(z, t) - \langle \rho_\theta(z, t) \rangle_t$, is used to estimate baroclinic pressure anomaly

$$p'(z, t) = g \int_z^0 \rho'_\theta(\zeta, t)\, d\zeta - \frac{g}{H} \int_{-H}^0 \int_z^0 \rho'_\theta(\zeta, t)\, d\zeta\, dz,$$

where g is the acceleration of gravity (taken as a constant 9.8 m s^{-2}) and the last term on the right-hand side forces $p'(z, t)$ to satisfy the baroclinicity condition (Kunze et al. 2002). An alternative formulation that expresses $p'(z, t)$ in terms of vertical displacement produces identical results.

Harmonic fits to short-duration perturbation time series isolate the semidiurnal signal. At each station, least squares fits of a time mean and semidiurnal sinusoids to $u'(z, t)$, $v'(z, t)$, $\xi'(z, t)$, and $p'(z, t)$ estimate semidiurnal fluctuations, for example,

$$\begin{aligned} \hat{u}(z, t) &= A(z) \cos(\omega t) + B(z) \sin(\omega t) + C(z) \\ &= Q(z) \cos[\omega t - \phi(z)] + C(z), \end{aligned}$$

where the caret indicates the semidiurnal fit, ω is the M_2 semidiurnal frequency 1.408×10^{-4} rad s^{-1}, amplitude $Q(z) = \sqrt{A(z)^2 + B(z)^2}$, phase $\phi(z) = \arctan[B(z)/A(z)]$, and $C(z)$ is the time mean. Averaged over all sites, semidiurnal fits contain 60% (50%) of the depth-averaged perturbation velocity (vertical displacement) variance, with individual station values of 30%–80%.

Semidiurnal fits of velocity and baroclinic pressure yield estimates of horizontal and vertical energy fluxes,

$$\begin{aligned} F_{E_u}(z) &= \langle \hat{u}(z, t) \hat{p}(z, t) \rangle_\phi, \\ F_{E_v}(z) &= \langle v'(z, t) \hat{p}(z, t) \rangle_\phi, \quad \text{and} \\ F_{E_w}(z) &= \langle \hat{w}(z, t) \hat{p}(z, t) \rangle_\phi, \end{aligned}$$

and profiles of horizontal and available potential energy density,

$$\mathrm{HKE}(z) = \frac{\rho_0}{2} \langle \hat{u}(z, t)^2 + v'(z, t)^2 \rangle_\phi \quad \text{and}$$

$$\mathrm{APE}(z) = \frac{\rho_0}{2} \overline{N(z)^2} \langle \xi(z, t)^2 \rangle_\phi,$$

where $\langle \rangle_\phi$ indicates averaging over one semidiurnal period and the overbar indicates a station average. Differentiation with respect to time of semidiurnal-fit vertical displacement $\hat{\xi}(z, t)$ yields semidiurnal vertical velocity $\hat{w}(z, t)$.

Near-inertial, broadband [i.e., Garrett–Munk (GM)], and mesoscale variability (Nash et al. 2005) contami-

nate semidiurnal harmonic fits to discretely sampled, short-duration time series. Error magnitude depends on the strength of contamination and the precise timing of sampling. By performing Monte Carlo simulations with synthetically generated M_2, near-inertial, and GM wave fields consistent with station 14, Nash et al. (2005) estimate depth-integrated energy-flux errors of 10%, with no systematic bias, for 20 kW m^{-1} energy flux sampled with six profiles over 15 hours.

To assess the error in our semidiurnal extractions, we employ the methods of Nash et al. (2006) and generate 100 synthetic time series at each station, each composed of randomly phased semidiurnal and GM wave fields consistent with the observed semidiurnal wave content.[1] Each realization was then sampled identically to the observations and semidiurnal fits performed to each synthetic profile time series, from which the energy flux, APE, and HKE were calculated. Standard errors were computed from the distribution of 100 realizations for each of these quantities (including semidiurnal amplitude and phase).

The analysis employs geographically oriented horizontal coordinates and stretched vertical coordinates. Along- and across-ridge coordinates ($\parallel$ and $\perp$) refer to an east–west system rotated clockwise 37° such that $x_\parallel$ points east-southeastward along the ridge and $y_\perp$ points north-northeastward across the ridge. Wentzel–Kramers–Brillouin (WKB) stretching and scaling normalize internal wave fields for the effects of variable stratification (Leaman and Sanford 1975). The stretched vertical coordinate is $z_{\text{wkb}} = \int_z^0 \overline{N(\zeta)}/N_0\, d\zeta$, where $N(z)$ is the buoyancy frequency, $N_0 = 2.5 \times 10^{-3}$ s^{-1} is the reference buoyancy frequency, and the overbar indicates a station average. Horizontal velocities and pressure scale as $(u_{\text{wkb}}, v_{\text{wkb}}, p_{\text{wkb}}) = (u, v, p)\sqrt{N_0/\overline{N(z)}}$, vertical velocity and displacement as $(w_{\text{wkb}}, \xi_{\text{wkb}}) = (w, \xi)\sqrt{\overline{N(z)}/N_0}$, and energy and energy flux as $(E_{\text{wkb}}, F_{E_{\text{wkb}}}) = (E, F_E)N_0/\overline{N(z)}$.

Modal decomposition follows from the vertical structure equation

$$\frac{d^2G_n(z)}{dz^2} + c_n[\overline{N^2(z)} - \omega^2]G_n(z) = 0,$$

with free-surface $[dG(0)/dz - gc_nG(0) = 0]$ and no-flow bottom boundary $[G(-H) = 0]$ conditions. Projections of semidiurnal fits $\hat{u}(z, t)$, $\hat{v}(z, t)$, $\hat{\xi}(z, t)$, and $\hat{p}(z, t)$ onto the first 50 vertical mode functions $G_n(z)$ were used to determine the mode contributions to HKE, APE, and energy flux. Averaged over all stations, the first five modes account for 98% of the vertically integrated energy flux. Because both velocity and pressure mode functions have surface maxima, the summed modes are unable to represent the vertical structure of profiles containing subsurface maxima.

The Princeton Ocean Model (POM; Blumberg and Mellor 1987) provides numerical results that aid interpretation of the observations and allow extrapolation over the ridge. Simulations were run for five domains along the ridge, three of which cover the region of AVP sampling (Fig. 1). Each domain has 4-km horizontal resolution and 51 vertical sigma levels that provide 60-m vertical resolution at 3000-m depth. The model employed Smith and Sandwell (1997) bathymetry, used the Mellor–Yamada 2.5-level subgrid-scale mixing parameterization for turbulence closure, and defined laterally uniform vertical stratification over each domain using historical data. The POM mode-splitting algorithm permits the use of a sponge layer at model boundaries to preferentially dampen outgoing baroclinic energy. The model produces an approximately linear representation of the combined M_2 and S_2 tides (Holloway and Merrifield 2003). Separate M_2- and S_2-forced simulations were thus summed to simulate spring–neap modulation, producing baroclinic currents and displacements at the times and locations of the AVP sites. Semidiurnal harmonic fits over a time span corresponding to that of AVP sampling provide M_2 energy-flux estimates at times and locations appropriate for comparison with the observations. Model standard errors were calculated as standard deviations across an ensemble consisting of the nine grid points closest to each AVP site.

4. Along-ridge internal tide variability—Observations and simulations

a. Semidiurnal amplitude and phase in energetic regions

Numerical simulations and observations reveal strong semidiurnal internal tides in the regions surrounding Kauai Channel and French Frigate Shoals (Fig. 1). Profiles of WKB-normalized cross-ridge velocity $\hat{v}_\perp$ and displacement $\hat{\xi}$ capture energetic fluctuations at a variety of vertical scales (Fig. 3). Estimates derived from small numbers of profiles typically exhibit large amplitude and phase uncertainties, with the largest

[1] Many stations lacked sufficient temporal resolution to isolate both semidiurnal and near-inertial signals simultaneously. However, Nash et al. (2005) show that harmonic analyses reject 90% of the near-inertial signal for sampling typical of these observations (~6 profiles over 15 h.) We therefore add only GM contamination and explicitly assume that error is only attributed to the relative phasing of the sampling with respect to the semidiurnal and GM wave fields. The GM wave fields were based on Cairns and Williams (1976), with depth-integrated $\text{APE}_{\text{GM}} = 3.1$ J m^{-2} and $\text{HKE}_{\text{GM}} = 5.0$ J m^{-2} based on a 3100-m water depth.

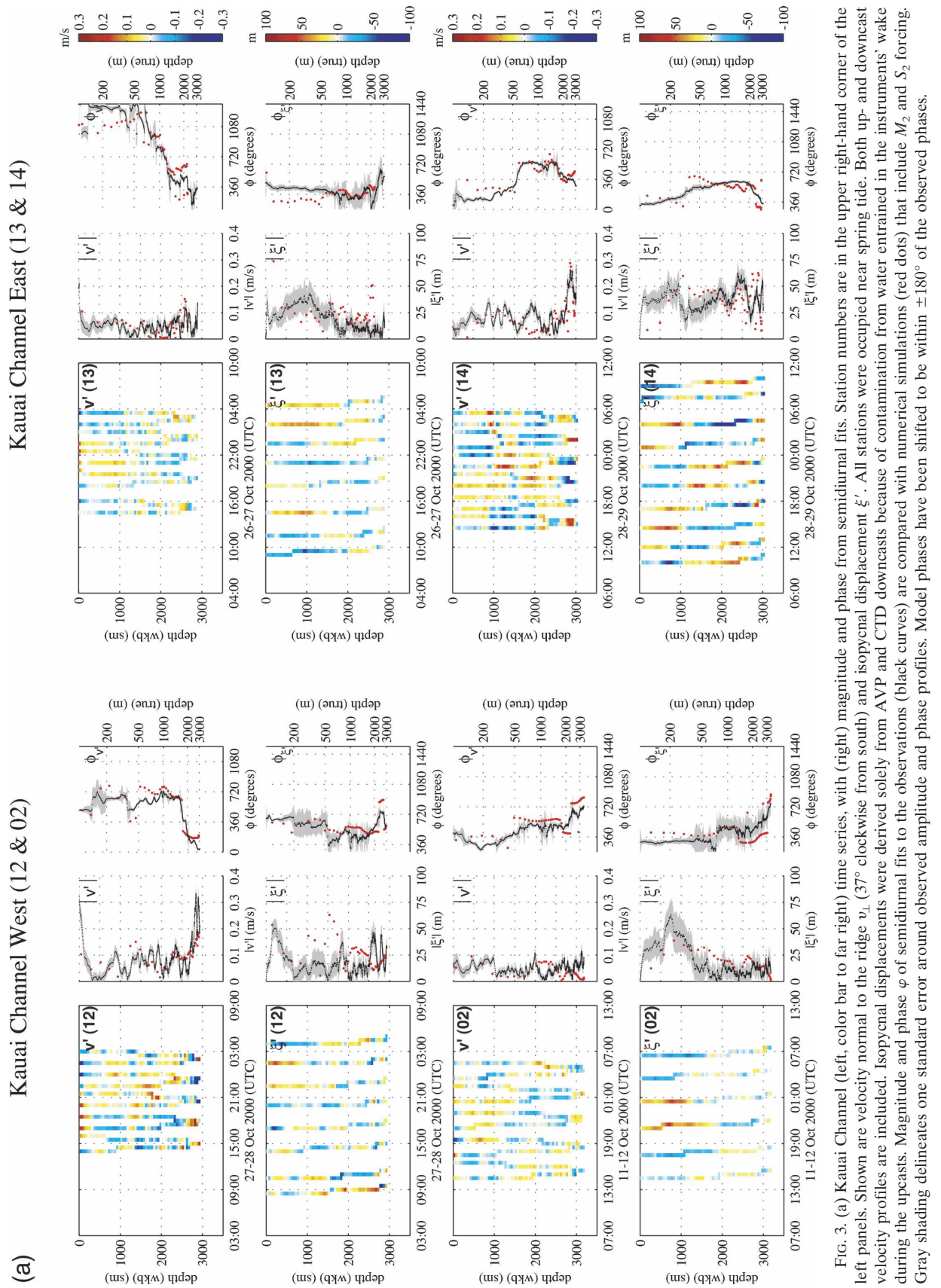

FIG. 3. (a) Kauai Channel (left, color bar to far right) time series, with (right) magnitude and phase from semidiurnal fits. Station numbers are in the upper right-hand corner of the left panels. Shown are velocity normal to the ridge $v_\perp$ (37° clockwise from south) and isopycnal displacement ξ'. All stations were occupied near spring tide. Both up- and downcast velocity profiles are included. Isopycnal displacements were derived solely from AVP and CTD downcasts because of contamination from water entrained in the instruments' wake during the upcasts. Magnitude and phase φ of semidiurnal fits to the observations (black curves) are compared with numerical simulations (red dots) that include M_2 and S_2 forcing. Gray shading delineates one standard error around observed amplitude and phase profiles. Model phases have been shifted to be within ±180° of the observed phases.

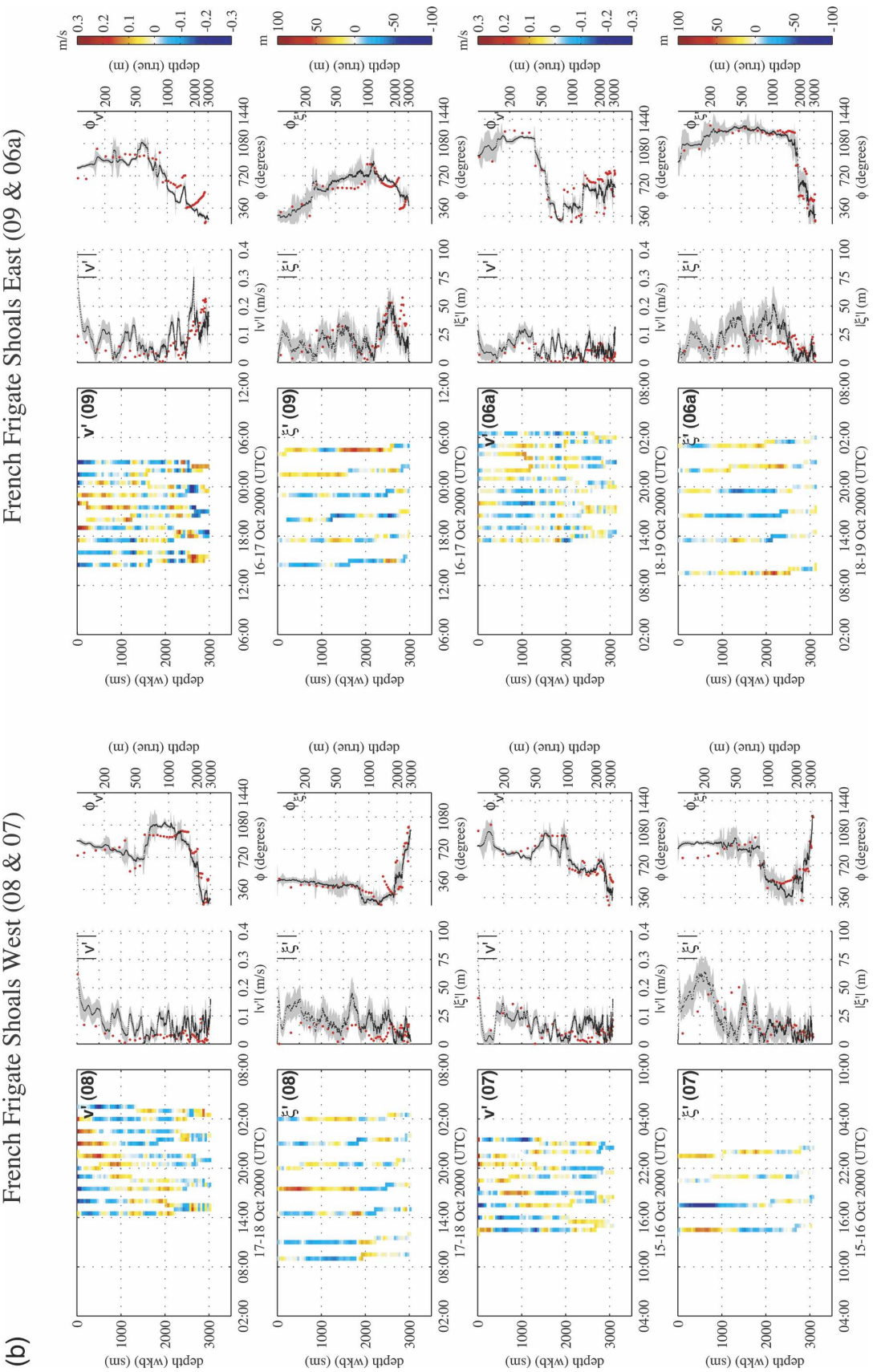

FIG. 3. (*Continued*) (b) As in (a) but for four stations (08, 07, 09, 06a) about French Frigate Shoals (Fig. 1).

phase errors occurring in regions of weak amplitude or large amplitude uncertainty. Observed phases (unwrapped to eliminate jumps exceeding 180° between adjacent depths) typically exhibit a combination of continuous phase change (implying vertical propagation) and abrupt jumps (indicating phase-locked superposition between up- and down-going waves), though the latter rarely occur at depths consistent with a mode-1 standing wave. Stations 06a and 14 provide the only exceptions. At these stations, $\hat{v}_\perp$ phase undergoes an abrupt mid-WKB-stretched depth phase shift with $\hat{\xi}$ phase showing little change, consistent with the structure expected for a mode-1 standing wave. At other stations, observed phase jumps near the surface and bottom boundaries may be produced by superpositions of incident and reflected waves. Stations 09, 12, and 14 reveal bottom-enhanced WKB-normalized cross-ridge velocity and, for station 09, displacement $\hat{\xi}$, where phase decreasing with depth implies downward energy propagation. At most sites, $\hat{v}_\perp$ and $\hat{\xi}$ exhibit complex amplitude and phase structures that differ markedly from each other, perhaps due to the superposition of multiple up- and down-going waves with differing wavelengths.

Modeled amplitude and phase (Fig. 3, red dots) agree roughly with observations (Fig. 3, black lines), though the model's limited vertical resolution prevents it from capturing the energetic high-wavenumber variability. Model phase has been offset by the difference between observed and modeled barotropic phase at each site. The model typically reproduces observed low-mode amplitude structure and occasionally captures smaller-scale features such as near-bottom $\hat{v}_\perp$ amplification at stations 09, 12, and 14. However, simulations fail to produce some large-scale amplitude peaks, such as the broad $\hat{\xi}$ maxima that occur above 1000 stretched meters (sm) (stations 02, 07, 08, and 13). Modeled phase change with depth $\partial\phi/\partial z$, which reflects internal wave vertical propagation, agrees with observations across broad vertical spans, though absolute offsets often approach 180°. The large range (over four complete cycles) used to display unwrapped phase (Fig. 3) sometimes masks differences between modeled and observed phase, making them appear more similar than they are.

b. Energy ratios

Depth-averaged energy ratios HKE/APE from the semidiurnal fits offer an additional diagnostic for assessing internal wave content and model performance. Observed ratios (Fig. 4a) fall around the value of 3 expected for the canonical Garrett and Munk (1979) internal wave spectrum with a slight bias toward the lower semidiurnal ratio of 1.33. The mode-1 contribution (Fig. 4b) provides greater contrast, with some stations falling near or below (elevated APE) the semidiurnal ratio and the rest near or above (elevated HKE) the Garrett–Munk ratio. This division in mode-1 behavior appears unrelated to station location, tidal phase, and fractional size of mode-1 contribution. Mode-2 contributions (Fig. 4c) scatter with less tendency to cluster near the GM ratio. Model energy ratios (Figs. 4d–f) cluster more closely around the semidiurnal value than the observations, perhaps due to the absence of forcing at frequencies other than tidal. Removing the barotropic APE component does not alter these results. A simple ridge generation model (Nash et al. 2006) finds high HKE/APE over the ridge crest and low HKE/APE on the flanks produced by coherent superposition of internal waves generated on opposite sides of the ridge. Numerical simulations show a similar pattern with large energy ratio gradients near the ridge. A superposition of waves traveling across the ridge in opposite directions can explain energy ratios that deviate from the semidiurnal intrinsic value, suggesting that the 3000-m isobath is close enough to the generation sites that the wave field consists of several phase-locked waves originating from multiple locations.

c. Energy fluxes

The geometry of the ridge should produce a shoaling beam near the surface and a plunging beam near the bottom (Pingree and New 1989, 1991; Nash et al. 2006). Observed and model energy-flux profiles from the eight stations around Kauai Channel and French Frigate Shoals show intensification in the upper ocean (Fig. 5), as expected from WKB scaling ($F_E \propto N$). However, the observations often exhibit near-surface intensification and energetic small-scale vertical structure that the model fails to capture, because of either inadequate vertical resolution in the model or sparse temporal sampling in the observations projecting energy from outside the semidiurnal band onto the semidiurnal fits (Nash et al. 2005). Our error estimates (Fig. 5) account for aliasing of GM energy that has significant depth dependence. High-wavenumber near-inertial energy similarly alters energy-flux profiles but was not accounted for because sampling was insufficient to resolve it. Observations also reveal near-bottom peaks in the cross-ridge energy flux ($F_{E_\perp}$) at some stations, though these rarely coincide with numerical predictions. Observed correlations $\langle v'p' \rangle / (\sqrt{\langle v'^2 \rangle}\sqrt{\langle p'^2 \rangle})$ of 0.3–0.7 in the energy-flux major-axis direction indicate that a large fraction of the water column variance contributes to the integrated flux. Correlations were <0.1 in the minor-axis direction.

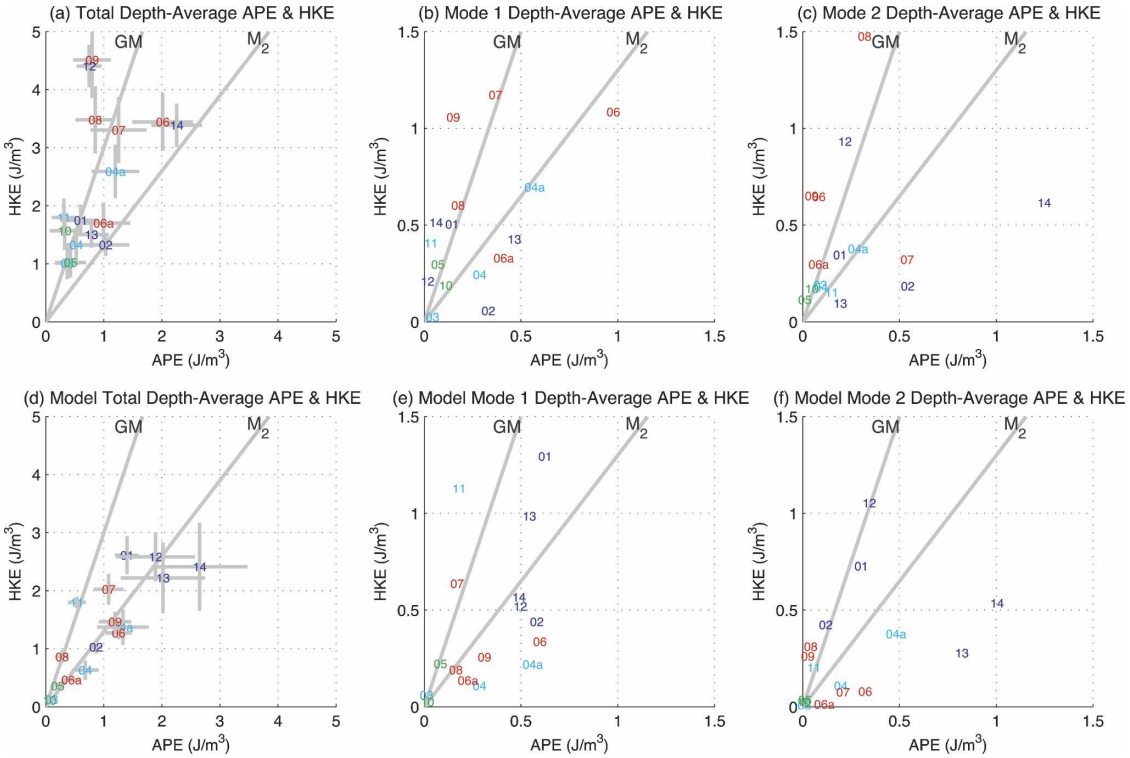

FIG. 4. Depth-integrated semidiurnal-fit (top) observed and (bottom) model energies (APE and HKE) labeled by station number. (a) Observed and (d) model total profile energies in all modes, (b) observed and (e) model contributions in mode 1, and (c) observed and (f) model contributions in mode 2. Gray bars mark one standard error around observed and modeled total depth-averaged APE and HKE. Diagonals correspond to GM and semidiurnal energy ratios HKE/APE.

Vertically integrated fluxes radiate north and south away from the Hawaiian Ridge in both observations and the model (Fig. 1), consistent with satellite altimetry (Ray and Mitchum 1997; Kantha and Tierney 1997) and farfield tomography (Dushaw et al. 1995) results that characterize the ridge as a source of internal tides. Observed energy-flux magnitudes range from 1 to 33 kW m^{-1} (Fig. 1, red; and Table 1) and follow the spatial pattern of high- and low-energy regions predicted by the model (Fig. 1, blue; and Table 1); errors in the observed depth-integrated energy flux average ± 2.5 kW m^{-1}. Strong fluxes emanate from French Frigate Shoals (9–33 kW m^{-1}), Kaena Ridge (4–18 kW m^{-1}), and the region west of Nihoa Island (3–15 kW m^{-1}), while weaker fluxes (0.4–2 kW m^{-1}) radiate from the regions east of Nihoa Island and near Necker Island. Observed and modeled fluxes typically point in the same direction at energetic sites, with the notable exception of stations 06 and 06a (southeast French Frigate Shoals) and 01 and 13 (west Kauai Channel) where observed fluxes exhibit a strong westward (along ridge) component not present in the simulations (Fig. 1). At most stations, mode 1 dominates both cross- and along-ridge energy fluxes (Fig. 1, bottom panels). Cross-ridge flux has significant mode-2 contributions at station 08 (northwest French Frigate Shoals) and stations 12 and 14 (Kauai Channel). Mode 2 dominates the along-ridge flux at station 02 (southwest Kauai Channel) and stations 07 and 09 (French Frigate Shoals).

Station occupation timing relative to the spring–neap cycle (Fig. 2) could explain some of the differences between high- and low-energy sites (Fig. 1 and Table 1). Model results (Holloway and Merrifield 2003) show significant spring–neap energy flux modulation, with spring fluxes roughly five times larger than those at neap (for locations close to the ridge). However, spatial patterns of high- and low-flux regions remain consistent through the spring–neap cycle. Observed energy fluxes west of Nihoa Island taken at neap (04) and spring (04a) tide show a fivefold increase consistent with model predictions. A similar comparison between sites 06 and 06a finds only a threefold increase, perhaps because 06a was occupied during the falling tide prior to the neap. Observed fluxes often exceed model values by a standard error at energetic sites (e.g., French Frigate Shoals) but agree more closely at low-energy sites

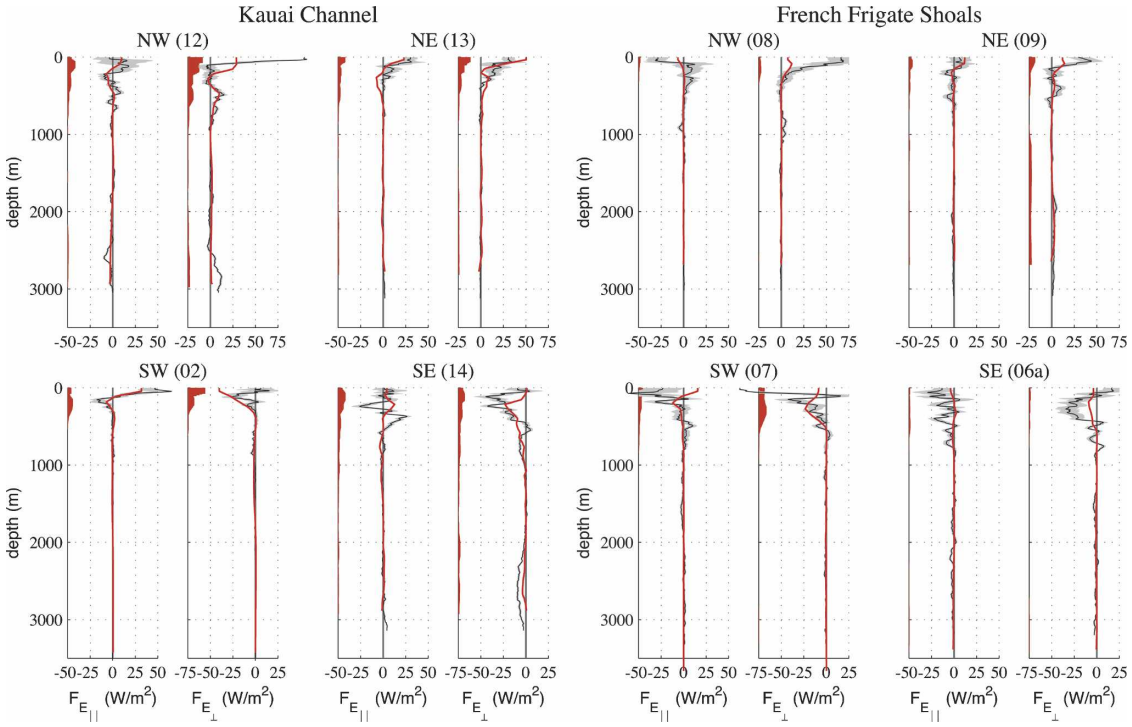

FIG. 5. Comparisons of across- and along-ridge energy fluxes F_E for the eight stations around Kauai Channel (12, 02, 13, 14) and French Frigate Shoals (08, 07, 09, 06a) shown in Fig. 3. Black lines mark AVP semidiurnal fit estimates and red lines the numerical simulations. Gray shading delineates one standard error around observed energy flux profiles. The length of the red bars extending from the left margin indicates one standard error for model energy-flux profiles. Both observed and model fluxes are concentrated in the upper water column, but the observations reveal greater vertical structure and are often stronger near the surface.

03 and 05. Model results reveal weak internal tide generation south of Necker Island, consistent with weak spring-tide energy flux observed at site 05. A fivefold energy flux increase from neap to spring tide implies spring energy fluxes of roughly 2 (11) kW m^{-1} at site 03 (10). Models and observations both depict weak energy fluxes radiating from the region east of Nihoa Island (03) but disagree at site 10 where relatively large neap-

TABLE 1. Observed (obs) and modeled (mod) depth-integrated cross-ridge (⊥), along-ridge (||), and energy-flux magnitude (kW m^{-1}) with standard errors.

Site	$F_{E\perp}$ (obs)	$F_{E\parallel}$ (obs)	$\lvert F_E\rvert$ (obs)	$F_{E\perp}$ (mod)	$F_{E\parallel}$ (mod)	$\lvert F_E\rvert$ (mod)
01	−5.0 ± 2.2	6.9 ± 2.6	8.5	−11.1 ± 1.3	6.6 ± 1.4	12.9
02	−3.2 ± 2.1	3.1 ± 1.9	4.5	−7.7 ± 0.6	2.8 ± 0.8	8.2
03	−0.2 ± 1.6	0.3 ± 1.5	0.4	−0.9 ± 0.1	0.5 ± 0.1	0.5
04	−0.8 ± 1.7	2.8 ± 1.8	2.9	−3.3 ± 0.6	1.3 ± 0.3	3.6
04a	−13.3 ± 3.5	7.8 ± 3.3	15.4	−6.4 ± 1.1	2.5 ± 0.8	6.9
05	−1.6 ± 1.8	1.0 ± 2.0	1.9	−1.7 ± 0.2	0.8 ± 0.2	1.9
06	−24.2 ± 5.9	−22.5 ± 4.8	33.0	−10.9 ± 1.1	−3.8 ± 1.5	11.5
06a	−9.3 ± 3.3	−8.2 ± 3.4	12.4	−3.7 ± 0.3	−1.2 ± 0.7	3.8
07	−12.5 ± 3.5	−5.0 ± 4.6	13.4	−7.2 ± 2.5	−0.5 ± 0.6	7.2
08	10.3 ± 3.5	0.5 ± 3.0	10.3	2.3 ± 0.3	−0.6 ± 0.4	2.4
09	8.6 ± 3.1	−1.8 ± 2.3	8.8	4.7 ± 3.4	0.7 ± 1.3	4.8
10	2.1 ± 1.4	0.9 ± 1.3	2.3	0.1 ± 0.1	−0.2 ± 0.1	0.2
11	4.4 ± 1.9	−0.5 ± 1.9	4.4	6.5 ± 0.6	−3.6 ± 0.6	7.4
12	13.5 ± 2.7	−0.9 ± 3.1	13.5	9.7 ± 1.5	−1.7 ± 0.8	9.8
13	6.4 ± 2.0	4.4 ± 1.9	7.8	7.9 ± 1.0	0.3 ± 0.6	7.9
14	−18.2 ± 2.8	2.3 ±2.1	18.3	−8.8 ± 0.8	1.4 ± 1.1	8.9

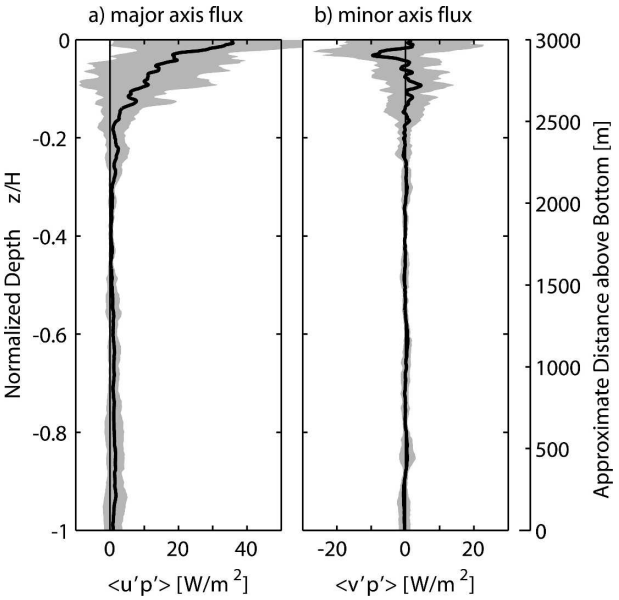

FIG. 6. Survey-wide average major-axis and minor-axis energy-flux profiles. Station profiles were rotated into the direction of the vertically integrated energy flux (major axis) before averaging. (left) Major-axis fluxes are positive at all depths, are surface-intensified, and approach zero near 1200 m. (right) Minor-axis fluxes are weaker, frequently reverse direction, and are of small vertical scale. Gray shading indicates the standard deviation calculated from all stations except site 01.

tide values imply large spring-tide energy flux radiating northward from Necker Island.

A composite energy-flux profile reveals major-axis fluxes oriented in the same direction over the entire water column (Fig. 6). The composite was generated by rotating each station into the direction of the vertically integrated energy flux, normalizing to a common depth range, and averaging over all stations. The shading indicates that individual station profiles deviate significantly from the station average. The resulting major-axis profile approaches zero at approximately 1200 m, deeper than the roughly 600-m mode-1 node depth. This, combined with near-surface energy-flux intensification, is consistent with profiles composed of additional modes beyond the first. At station 14 (on the flank south of Kaena Ridge), the three-dimensional energy-flux vector (e.g., Nash et al. 2006) suggests that the internal tide consists of a shoaling beam in the upper ocean and a plunging beam in the deep water. The observations presented here do not capture a similar structure at the other stations.

With the exception of cross-ridge energy flux, and to some degree APE, observed semidiurnal fit and modeled vertically averaged HKE, APE, and energy fluxes ($F_{E_\perp}$,$F_{E||}$) show only weak agreement. Observed cross-ridge energy fluxes equal or exceed (within one standard error) those produced by the model at all stations except 01, 02, and 04 ($F_{E_\perp}$, Fig. 7c), suggesting that depth-integrated fluxes could be a factor of 2 larger than predicted by the simulations. Similarly, the model predicts smaller along-ridge fluxes ($F_{E||}$, Fig. 7d) than observed (e.g., French Frigate Shoals stations 06 and 06a). Modeled HKE falls below observed at all but two sites (01 and 13) (Fig. 7a), while modeled and observed APE are identical (within one standard error) at 10 of the 16 stations (Fig. 7b). Several factors may contribute to these differences, including

1) inadequately resolved model bathymetry and near-boundary dynamics (both bottom and surface);
2) radiation from other generation sites, in particular from outside the model domains (Fig. 1);
3) aliasing of internal wave variability outside the semidiurnal (e.g., near inertial, GM) into the observed energy flux, HKE, and APE estimates; and
4) internal tide interactions with mesoscale flows not included in the model. The influence of mesoscale interactions will be most significant far from the generation regions over the ridge (Rainville and Pinkel 2006). Because AVP sites were situated close to generation regions, the effects of mesoscale modulation should play a small role on propagated fields. However, mesoscale-induced changes in the background stratification from their climatological mean may significantly alter generation locations.

The rough factor-of-2 agreement between observed and model cross-ridge energy fluxes (Figs. 1 and 7c) motivates an integration along the 2000-km length of the Hawaiian Ridge in the model. The model's M_2 semidiurnal surface tide loss is 15 ± 7 GW with 10 GW radiated away (6 GW in mode 1; Merrifield and Holloway 2002). Egbert and Ray (2001) suggest 20 ± 6 GW surface tide loss at the ridge. The SHA 10-layer numerical model gets 24-GW conversion for all tides, Niwa and Hibiya (2001) 15 GW for M_2, and Morozov (1995) 8 GW in M_2 using a simplified Baines (1982) theory. The idealized knife-edge model of St. Laurent et al. (2003) predicts 22 GW. Ray and Cartwright (2001) estimate that 6 GW radiates away in mode 1 based on satellite altimetry, consistent with our estimate. Even given the uncertainties, this implies a remarkably imperturbable, coherent, near-ridge mode-1 internal tide because the satellite estimates are based on phase-locked fits over 9 years of data. Dushaw (2002) get a smaller 2.6 ± 0.5 GW over a 1700-km integral based on an objective map of satellite altimetry, which is attributed to smoothing by objective analysis. Two-layer numerical simulations find 5.4 GW (Kang et al. 2000), though missing the Kauai Channel contribution, and 15

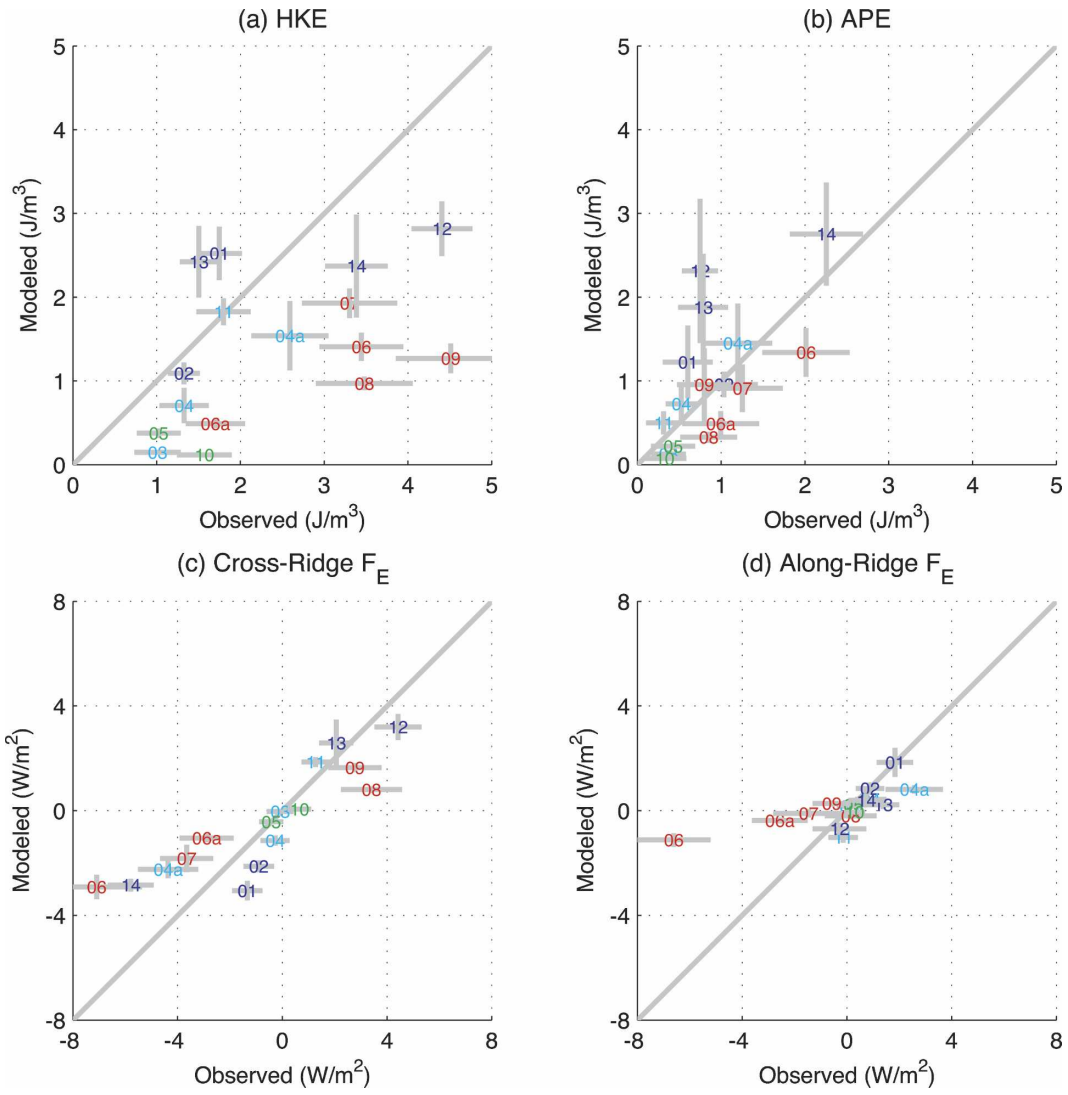

FIG. 7. Modeled vs observed (a) vertically averaged horizontal kinetic energy HKE, (b) vertically averaged available potential energy APE, (c) vertically averaged cross-ridge energy flux, and (d) vertically averaged along-ridge energy flux labeled by station number. Gray bars mark one standard error around each estimate. Modeled and observed cross-ridge energy fluxes agree to within a factor of 2. Modeled HKE is often smaller than that observed, while modeled and observed APE are often within one standard error of agreement.

GW (SHA) radiating away. Klymak et al. (2006) infer that 3 ± 1.5 GW is dissipated turbulently within 60 km of the ridge, 80% of this inside the 3000-m isobath. Moving away from the ridge, Chiswell (2002) estimates 4.4 kW m^{-1} based on measurements at station Aloha, a number comparable to the flux at that location in the numerical model of SHA.

5. Turbulent mixing

Turbulent kinetic energy dissipation rates ε were computed spectrally over 5-m depth intervals using the AVP microscale shear probe not contaminated by the drop-weight wake (see appendix). In the following, 5-m dissipation rates contaminated by noise were set to zero so that average $\langle\varepsilon\rangle$ represent conservative minima, biased low by at most 30%. Average diapycnal eddy diffusivities $\langle K\rangle = \gamma\langle\varepsilon\rangle/N^2$ (Osborn 1980) were computed based on $\langle\varepsilon\rangle$, the mean stratification $\overline{N^2}$, and a mixing efficiency $\gamma = 0.2$ (Oakey 1982; Moum 1996). These were then bin averaged into 100-m depth intervals.

Survey-averaged dissipation rates $\langle\varepsilon(z)\rangle$ have a maximum exceeding 10^{-7} W kg^{-1} in the upper 100 m, diminishing to $\sim 5 \times 10^{-10}$ W kg^{-1} at 1500-m depth (1500

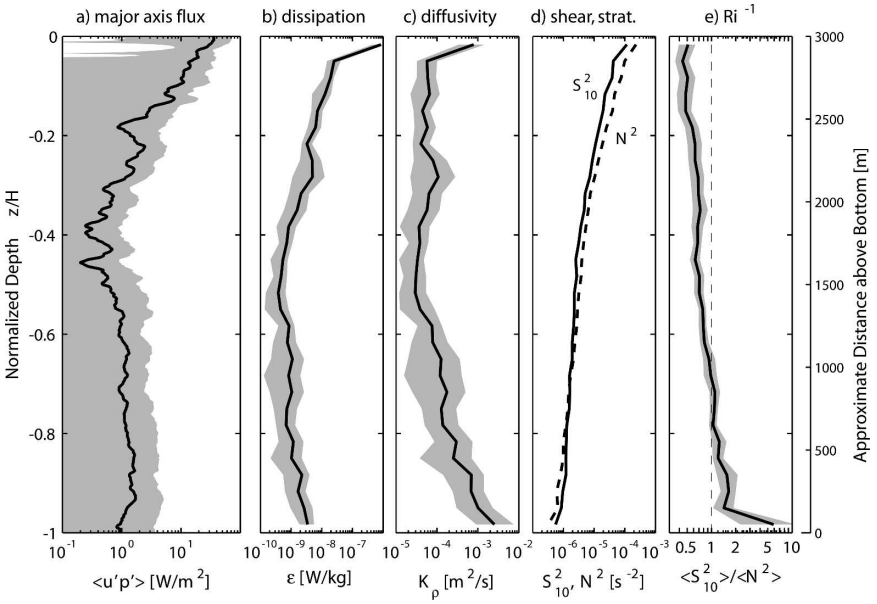

FIG. 8. Survey-averaged WKB-scaled major-axis energy flux $\langle v_\perp' p' \rangle$, dissipation rate $\langle \varepsilon \rangle$, diapycnal eddy diffusivity $\langle K \rangle$, shear variance $\langle S^2 \rangle$, stratification $\langle N^2 \rangle$, and 10-m inverse Richardson number $\mathrm{Ri}^{-1} = \langle S^2 \rangle / \langle N^2 \rangle$ profiles. Note that depth is not WKB stretched in this figure. To remove small differences in bottom depth (stations were nominally at 3000-m depth, and all but two had $3000 < H < 3500$ m), data are plotted against fractional water depth. Because all the stations were close to the 3000-m isobath, the approximate height above bottom is shown on the right.

mab), then gradually increasing to 3×10^{-9} W kg^{-1} near the bottom (Fig. 8b). Stratified turbulence bottom boundary layers with $\langle \varepsilon(z) \rangle = 10^{-8} - 10^{-7}$ W kg^{-1} were observed in the bottom 50–200 m at many stations, as commonly found over rough topography (Nabatov and Ozmidov 1988; Toole et al. 1997; Lueck and Mudge 1997; Kunze and Toole 1997; Lien and Gregg 2001; Ledwell et al. 2000; Lozovatsky et al. 2003; Nash et al. 2004). Eddy diffusivity $\langle \mathrm{K}(z) \rangle$ is $(0.5–1.0) \times 10^{-4}$ m^2 s^{-1} between the surface and 1800 m (1200 mab), exponentially increasing below to 20×10^{-4} m^2 s^{-1} near the bottom (Fig. 8c). Using a turbulence structure function, Klymak et al. (2006) find diffusivities averaged across the ridge of 3×10^{-5} m^2 s^{-1} at all depths.

In the ocean interior, well away from topography, eddy diffusivity is typically $(0.05–0.1) \times 10^{-4}$ m^2 s^{-1}, independent of depth (Gregg 1989; Ledwell et al. 1993; Toole et al. 1994; Kunze and Sanford 1996; Mauritzen et al. 2002). Thus, main pycnocline diffusivities around the Hawaiian Ridge are an order of magnitude higher than typical open-ocean values. Near-bottom diffusivities are elevated by over two orders of magnitude from those typical of the ocean interior. Comparably high near-bottom diffusivities are found in stratified turbulent boundary layers extending several hundred meters over other rough topography, where tide–topography interactions have been implicated. However, $O(10^{-4}$ m^2 s^{-1}) diffusivities have not previously been reported to be so pervasive in the upper water column. The 10-m inverse Richardson number $\langle S^2 \rangle / \langle N^2 \rangle$ (Fig. 8f) increases with depth from 0.3 in the upper pycnocline to 1.5 near the bottom due to increasing shear, then increases sharply in the bottom 100 mab.

Microstructure dissipation rates are consistent to within a factor of 2 with estimates using the finescale shear-based Gregg–Henyey parameterization (Henyey et al. 1986; Gregg 1989) over more than two decades from 5×10^{-10} to 10^{-7} W kg^{-1} (Fig. 9). Below 5×10^{-10} W kg^{-1}, microstructure estimates are high, likely because of measurement noise. Above 5×10^{-8} W kg^{-1}, microstructure estimates are also high, but there are few data. The Gregg–Henyey parameterization is based on the transfer of energy through the vertical wavenumber spectrum to small scales by internal wave–wave interactions. Rough agreement between observed dissipation rates and the parameterization (Fig. 9) suggests that, even as close as the 3000-m isobath, these small-scale interactions participate in the cascade to turbulence production on the ridge flanks. The Gregg–Henyey scaling was also found to be effective in the

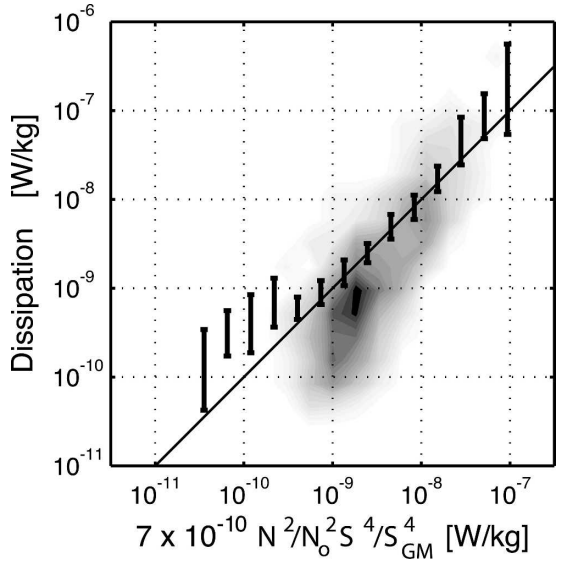

FIG. 9. Observed microstructure dissipation rate ε vs predictions from the Gregg–Henyey finescale shear parameterization. Gray shading in the background represents the probability distribution of 5-m microstructure dissipation rates. Vertical error bars correspond to 95% confidence limits about bin-averaged microstructure dissipation rates ε. There are very few data for $N^2/N_0^2S^4/S_{\rm GM}^4$ below 5×10^{-10} W kg^{-1} and above 5×10^{-8} W kg^{-1}, so averages in these ranges are suspect. Except for $\varepsilon < 5 \times 10^{-10}$ W kg^{-1}, where microscale noise appears to limit the minimum value on the horizontal axis to $O(10^{-9}$ W kg$^{-1})$, the parameterization is consistent with microstructure values to within a factor of 2.

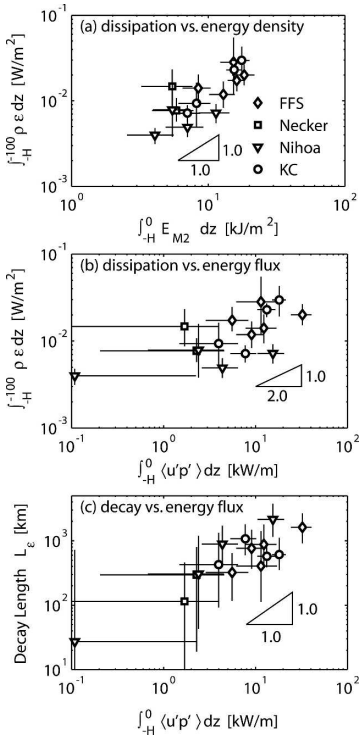

FIG. 10. Depth-integrated dissipation rate $\int_{-H}^{-100} \rho\varepsilon\, dz$ vs depth-integrated (top) semidiurnal energy $\int_{-H}^{0}$ (HKE + APE) dz and (middle) energy-flux magnitude $|\int_{-H}^{0} \langle \mathbf{v}'p' \rangle_\phi\, dz|$, as well as (bottom) decay length $L_\varepsilon = |\int_{-H}^{0} \langle \mathbf{v}'p' \rangle_\phi\, dz| / \int_{-H}^{-100} \varepsilon\, dz$ vs depth-integrated energy-flux magnitude. The depth-integrated energy flux excludes the surface 100 m where high stratification and numerous other processes contaminate the estimate. The decay length is inferred by dividing the magnitude of the vertically integrated energy flux by the vertically integrated dissipation rate and is likely an underestimate because high dissipation rates are concentrated near the ridge (Klymak et al. 2006). Higher turbulent dissipation rates are associated with higher energies and higher energy fluxes. Longer decay lengths are associated with higher energy fluxes.

stratified turbulent boundary layer overlying a corrugated continental slope (Nash et al. 2004).

Depth-integrated dissipation rate $\int_\varepsilon = \int_{-H}^{-100} \rho\varepsilon\, dz$ is correlated with depth-integrated energy $\int_{-H}^{-100} E\, dz$ (Fig. 10a) and energy flux $\rho_0 \int_{-H}^{-100} \langle \mathbf{v}'p' \rangle\, dz$ (Fig. 10b). The relationship between dissipation and energy density is consistent with the $\varepsilon \sim E^{1\pm0.5}$ derived by Klymak et al. (2006). Since high-wavenumber shear scales with E, it is expected that ε be related to the energy density. However, turbulent dissipation is only weakly related to energy flux (dissipation roughly scales as $\varepsilon \sim F_E^{0.5}$), possibly because the low modes dominate F_E and flux may be weak in regions where energetic waves oppose each other (Nash et al 2006). Though these integrations omit the upper 100 m to avoid surface-forced turbulence, depth-integrated dissipation rates are dominated by values in the upper 1000 m, even in profiles that exhibit near-bottom intensification. On average, only 12% of the integrated dissipation occurs below 1000 m. Even at the most bottom-intensified station (12, northwest of Kauai Channel) only 40% occurs below 1000 m. Dividing energy flux by dissipation rate (Fig. 10c) yields a decay length scale of 100–2000 km. This is an underestimate of the actual decay scale of the internal tide, as the calculation assumes uniform dissipation over this length scale, while Klymak et al. (2006) find that the highest dissipation rates are concentrated near the ridge.

6. Conclusions

Semidiurnal tides radiating away from the Hawaiian Ridge dominate full-depth profile measurements conducted along the 3000-m isobath north and south of the crest (Fig. 1 and Table 1). Internal tide generation appears to be highly heterogeneous, with the strongest cross-ridge energy fluxes at French Frigate Shoals (9–33 kW m^{-1}), Kaena Ridge in Kauai Channel (4–18 kW m^{-1}), and west of Nihoa Island (3–15 kW m^{-1}). Weak cross-ridge fluxes (0.4–2 kW m^{-1}) radiate from Necker

and Nihoa Islands (Fig. 6). Observed spatial patterns agree with those produced by a numerical simulation of M_2 and S_2 semidiurnal surface tide currents interacting with Hawaiian Ridge topography. Model results integrated along the ridge also agree with previous estimates of surface tide loss and low-mode internal tide radiation from the Hawaiian Ridge.

While model and observed depth-integrated cross-ridge energy fluxes agree to within a factor of 2, the observations find larger along-ridge energy fluxes at some stations (Fig. 7), particularly those near model domain boundaries (Fig. 1). Observed semidiurnal horizontal kinetic energies are higher than predicted by the model, while observed and model semidiurnal available potential energies are often similar. We interpret these results, as well as the complicated phase structure (Fig. 3), as due to a superposition of many semidiurnal waves of various wavelengths and directions of propagation constructively and destructively interfering with each other. Maps of vertically averaged energies and energy ratios from the model (not shown) reveal considerable lateral variability in close proximity to the ridge that likely arises from the coherent superposition of newly generated waves from different sources on either side of the ridge. Particularly strong model lateral gradients are found close to many AVP stations. The comparison of energy-flux profiles (Fig. 5) suggests greater near-surface intensification in the observations than in the model. Possible reasons for these differences include

1) coarse (~60 m) model vertical resolution that cannot capture details of the vertical structure, particularly near the surface;
2) inadequately resolved model bathymetry, which could play an important role due to geometric sensitivities of the generation mechanism; and
3) radiation from generation sites outside the numerical domains, which may explain differences in along-ridge energy fluxes.

Eddy diffusivities increase exponentially from $O(10^{-4}\ \mathrm{m^2\ s^{-1}})$ in the upper 1800 m to $20 \times 10^{-4}\ \mathrm{m^2\ s^{-1}}$ at the bottom; this near-boundary intensification in stratified turbulence is reminiscent of similar features found over other rough topography. Turbulence levels are consistent with the predictions of a finescale parameterization (Gregg 1989). Assuming interior (away from bathymetry) diffusivities of $0.1 \times 10^{-4}\ \mathrm{m^2\ s^{-1}}$, observed near-bottom enhancement could, at most, double North Pacific basin-average (above 4000 m) diffusivity given the basin's hypsometry (Kunze and Toole 1997). Specifically, local topographic enhancement of turbulent mixing associated with the Hawaiian Ridge is insufficient to raise the basin-average eddy diffusivity to the canonical $10^{-4}\ \mathrm{m^2\ s^{-1}}$. Modest average diffusivities of $O(10^{-4}\ \mathrm{m^2\ s^{-1}})$ over all depths near the Hawaiian Ridge (Klymak et al. 2006) support this finding.

Only a small fraction of the estimated 20 ± 6 GW surface tide loss (Egbert and Ray 2001) is locally available for abyssal mixing. Observations find 3 ± 1.5 GW dissipated with 80% of the loss occurring inside of the 3000-m isobath (Klymak et al. 2006). Of the 2.4 GW dissipated near the generation region, observed dissipation rates (e.g., Fig. 8) suggest that only 12% dissipates below 1000 m. Thus, closer to 2%, rather than the 50% of surface tide loss suggested by Munk and Wunsch (1998), is available for local abyssal mixing. Of course, if the radiated portion dissipates at great depth, it could still contribute substantially to abyssal mixing. At the Mendocino Escarpment, one-half of the radiated energy flux was lost in the upper ocean at the first surface reflection (Althaus et al. 2003) through turbulent losses (not measured) or through scattering into less coherent modes. This was not found for the Hawaiian Ridge radiated field though, as already noted, dissipation was still concentrated in the main pycnocline. Amplitudes, and hence nonlinearity, will tend to be larger in the strongly stratified upper ocean. This includes parametric subharmonic instability, which has been proposed as a mechanism for transferring energy rapidly from semidiurnal frequencies into turbulence at these latitudes (Niwa 1998; Hibiya et al. 2002, MacKinnon and Winters 2005, unpublished manuscript). The two mechanisms that could transfer tidal energy to small scales in the abyss are (i) critical reflection where bottom slopes match ray path slopes (Eriksen 1982; Nash et al. 2004), unlikely because ray paths are steep in weak abyssal stratification), and scattering from (ii) large-scale topographic features (Johnston and Merrifield 2004) and (iii) small-scale topographic features, which St. Laurent and Garrett (2002) suggest is only 10% efficient.

Acknowledgments. The authors thank John Dunlap, Art Bartlett, Bob Drever, Eric Boget, Dicky Allison, Alana Althaus, and the captain and crew of the R/V *Wecoma* for their able assistance with the data collection. Yvonne Firing provided helpful guidance for interpreting the numerical results. This work was supported by NSF Grant OCE 98-19537.

APPENDIX

Microstructure Analysis

The dissipation rate ε was inferred from microscale shear measured with two shear probes located 15 cm

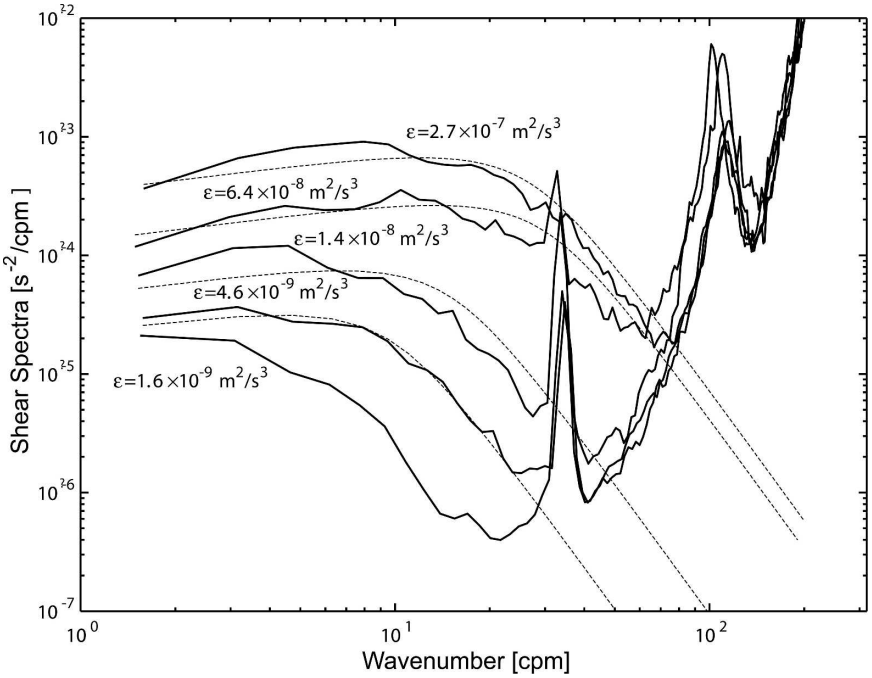

FIG. A1. Velocity shear (u_z, v_z) spectra for five patches of turbulence (solid) along with the corresponding Nasmyth (1970) empirical form (dotted). In order of increasing dissipation rates: (i) AVP 764 (2100–2150 m); (ii) AVP 764 (3020 m); (iii) AVP 764 (370–385 m); (iv) AVP 764 (45–75 m); and (v) AVP768 (2730–2780 m).

from the AVP centerline and sampled at 416.7 Hz. These were angled so that their axes were aligned with the oncoming flow (AVP rotates at 0.2 revolutions per second so that the probes trace a helical path). The dissipation rate is estimated assuming isotropy so that $\varepsilon = 7.5\nu\langle u_z^2\rangle$, where u represents the measured horizontal velocity component at dissipation (viscous) length scales and u_z its vertical derivative. Sample spectra from five 15–50-m turbulent patches are shown in Fig. A1. Apart from narrowband noise peaks, these shear spectra are well resolved and agree well with an empirical form (Nasmyth 1970; Oakey 1982). Noise peaks appear near the 33-Hz vibrational frequency of the Sea-Bird pump (30–35 cpm for AVP 1 m s^{-1} fall speed) and near 100 cpm (Fig. A1). Following Wesson and Gregg (1994), we avoid noise from these narrowband peaks in the dissipation rate calculation by integrating shear variance below 30 cpm. Nasmyth (1970) empirical spectra were fit to the resolved wavenumber band of the spectra and used to correct for lost variance at high wavenumbers.

Several sources of noise limited our ability to measure weak turbulence ($<10^{-10}$ W kg^{-1}). Two drop weights hung 0.5 and 2 m below the sensors. The wake from these often contaminated the shear probe signals. Fortunately, the wake only affected one probe at a time, so contamination was readily identified by dissipation rates of 10^{-5}–10^{-4} W kg^{-1} in one but not the other probe. The other probe typically had 5-m dissipation rates ε below 5×10^{-9} W kg^{-1} over depth intervals of hundreds of meters, and these numbers were used for the dissipation calculation. We use these data to measure the noise floor for ε.

Sources of noise include (i) proximity of the probes to the turbulent wake generated by the drop weights, (ii) mechanical vibrations, and (iii) pinging of the AVP acoustic Doppler. Broadband hydrodynamic noise and low-frequency vibrations of the instrument, which cannot easily be distinguished from turbulence, set the noise floor $\varepsilon_{\min}$. The minimum dissipation rate detectable by AVP remained constant with depth but varied from drop to drop, likely because of subtle differences in the drop-weight configurations. This noise floor was estimated by choosing a weakly turbulent layer below 500-m depth from each profile. The probability distribution function (pdf) of 5-m dissipation rate in this layer was then computed to characterize the noise $\varepsilon_{\text{noise}}$. A sample pdf shown in Fig. A2 is dominated by lognormal noise because most deep oceanic dissipation rates are less than 5×10^{-9} W kg^{-1}. The high dissipation rate tail represents ocean turbulence. An iterative procedure, which retained only $\varepsilon_{\text{noise}}$ estimates within

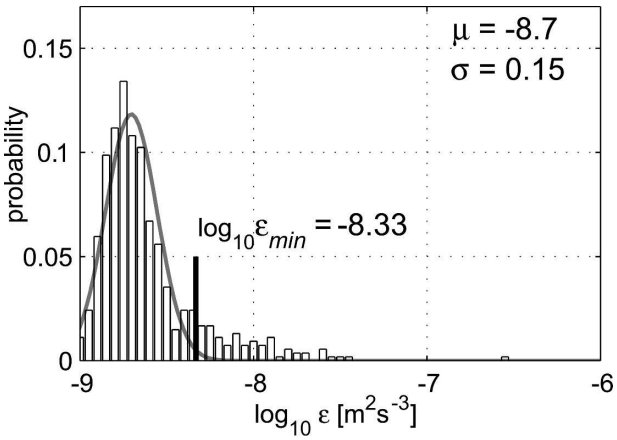

FIG. A2. Noise floor estimation for AVP drop 721. The mean μ and standard deviation σ of $\log(\varepsilon_{\text{noise}})$ were iteratively computed for those estimates within 2.5σ of the mean μ. The shaded curve represents the final lognormal noise distribution and the solid vertical bar the noise floor.

2.5 standard deviations (σ) of the mean of $\log(\varepsilon_{\text{noise}})$, was then used to set the noise threshold as $\log(\varepsilon_{\min}) = \langle\log(\varepsilon_{\text{noise}})\rangle + 2.5\sigma$. Any 5-m dissipation rates above $\varepsilon_{\min}$ were considered uncontaminated signal and retained in the 100-m averages, while those below were assumed to be noise and set to zero. It is inevitable that some turbulent signal will be discarded by the above procedure, but it allows determination of a conservative lower-bound dissipation rate. The noise floor varied from profile to profile, ranging from 3×10^{-9} to 3×10^{-8} W kg^{-1} with an average of 8×10^{-9} W kg^{-1}.

As a check, the 5-m dissipation rates were averaged in two ways: (i) simply averaging the raw 5-m ε, regardless of the noise floor, to obtain an upper-bound average dissipation rate $\varepsilon_{\max}$ and (ii) setting values below the noise floor to zero before averaging to get a lower-bound dissipation rate $\varepsilon_{\min}$. Depth-averaged minimum dissipation rates $\varepsilon_{\min}$ were rarely below one-half of the depth-averaged $\varepsilon_{\max}$ for all six station occupations. Using either method does not bias the bulk dissipation rates by more than 30%. However, the average dissipation rate is usually dominated by a few large events, so $\varepsilon_{\min}$ provides the more appropriate conservative estimate of $\langle\varepsilon\rangle$. Because a relatively small number of strong events dominate turbulence averages, 100-m estimates of $\varepsilon_{\min}$ can realistically fall below the AVP noise floor.

REFERENCES

Althaus, A. M., E. Kunze, and T. B. Sanford, 2003: Internal tide radiation from Mendocino Escarpment. *J. Phys. Oceanogr.,* **33,** 1510–1527.

Avicola, G. S., J. N. Moum, J. M. Klymak, J. D. Nash, M. D. Levine, and D. S. Luther, 2003: Localized regions of elevated dissipation over the Hawaiian Ridge: Preliminary findings. *Eos, Trans. Amer. Geophys. Union,* **84,** OS39.

Baines, P. G., 1982: On internal tide generation models. *Deep-Sea Res.,* **29,** 307–338.

Blumberg, A. F., and G. L. Mellor, 1987: A description of a three-dimensional coastal ocean model. *Three-Dimensional Coastal Ocean Models,* N. S. Heaps, Ed., Coastal Estuarine Studies, Vol. 4, Amer. Geophys. Union, 1–16.

Cairns, J. L., and G. O. Williams, 1976: Internal wave observations from a midwater float, 2. *J. Geophys. Res.,* **81,** 1943–1950.

Carter, G. S., and M. C. Gregg, 2003: Turbulence near a small seamount on the Kaena Point Ridge, Hawaii. *Eos, Trans. Amer. Geophys. Union,* **84,** OS39.

Chiswell, S. M., 2002: Energy levels, phase and amplitude modulation of the baroclinic tide off Hawaii. *J. Phys. Oceanogr.,* **32,** 2640–2651.

Cummins, P. F., J. Y. Cherniawski, and M. G. G. Foreman, 2001: North Pacific internal tides from the Aleutian Ridge: Altimeter observations and modeling. *J. Mar. Res.,* **59,** 167–191.

Desaubies, Y., and M. C. Gregg, 1981: Reversible and irreversible finestructure. *J. Phys. Oceanogr.,* **11,** 541–556.

Dushaw, B. D., 2002: Mapping low-mode internal tides near Hawaii using TOPEX/Poseidon altimeter data. *Geophys. Res. Lett.,* **29,** 1250, doi:10.1029/2001GL013944.

——, 2003: Mapping and wavenumber resolution of line-integral data for observations of low-mode internal tides. *J. Atmos. Oceanic Technol.,* **20,** 1043–1059.

——, B. D. Cornuelle, P. F. Worcester, B. M. Howe, and D. S. Luther, 1995: Barotropic and baroclinic tides in the central North Pacific Ocean determined from long-range reciprocal acoustic transmissions. *J. Phys. Oceanogr.,* **25,** 631–647.

Egbert, G. D., and R. Ray, 2001: Estimates of M_2 tidal energy dissipation from TOPEX/Poseidon altimeter data. *J. Geophys. Res.,* **106,** 22 475–22 502.

Eriksen, C. C., 1982: Observations of internal wave reflection off sloping bottoms. *J. Geophys. Res.,* **87,** 525–538.

Finnigan, T. D., D. S. Luther, and R. Lukas, 2002: Observations of enhanced diapycnal mixing near the Hawaiian Ridge. *J. Phys. Oceanogr.,* **32,** 2988–3002.

Garrett, C., and W. Munk, 1979: Internal waves in the ocean. *Annu. Rev. Fluid Mech.,* **11,** 339–369.

Gregg, M. C., 1989: Scaling turbulent dissipation in the thermocline. *J. Geophys. Res.,* **94,** 9686–9698.

Henyey, F. S., J. Wright, and S. M. Flatte, 1986: Energy and action flow through the internal wave field: An eikonal approach. *J. Geophys. Res.,* **91,** 8487–8495.

Hibiya, T., M. Nagasawa, and Y. Niwa, 2002: Nonlinear energy transfer within the ocean internal wave spectrum at mid and high latitudes. *J. Geophys. Res.,* **107,** 3207, doi:10.1029/2001JC001210.

Holloway, P. E., and M. A. Merrifield, 1999: Internal tide generation by seamounts, ridges and islands. *J. Geophys. Res.,* **104,** 25 937–25 951.

——, and ——, 2003: On the spring–neap variability and age of the internal tide at the Hawaiian Ridge. *J. Geophys. Res.,* **108,** 3126, doi:10.129/2002JC001486.

Jeffries, H., 1920: Tidal friction in shallow seas. *Philos. Trans. Roy. Soc. London,* **A221,** 239–264.

Johnston, T. M. S., and M. A. Merrifield, 2004: Internal tide scattering at seamounts, ridges, and islands. *J. Geophys. Res.,* **108,** 3180, doi:10.1029/2002JC001528.

——, ——, and P. E. Holloway, 2003: Internal tide scattering at

the Line Islands Ridge. *J. Geophys. Res.,* **108,** 3365, doi:10.1029/2003JC001844.

Kang, S. K., M. G. G. Foreman, W. R. Crawford, and J. Y. Cherniawsky, 2000: Numerical modeling of internal tide generation along the Hawaiian Ridge. *J. Phys. Oceanogr.,* **30,** 1083–1098.

Kantha, L. H., and C. C. Tierney, 1997: Global baroclinic tides. *Progress In Oceanography,* Vol. 40, Pergamon, 163–178.

Klymak, J. M., and Coauthors, 2006: An estimate of tidal energy lost to turbulence at the Hawaiian Ridge. *J. Phys. Oceanogr.,* **36,** 1148–1164.

Kunze, E., and T. B. Sanford, 1996: Abyssal mixing: Where it is not. *J. Phys. Oceanogr.,* **26,** 2286–2296.

——, and J. M. Toole, 1997: Tidally driven vorticity, diurnal shear, and turbulence atop Fieberling Seamount. *J. Phys. Oceanogr.,* **27,** 2663–2693.

——, L. K. Rosenfeld, G. S. Carter, and M. C. Gregg, 2002: Internal waves in Monterey Submarine Canyon. *J. Phys. Oceanogr.,* **32,** 1890–1913.

——, T. B. Sanford, and C. M. Lee, 2003: Internal tide energetics in Kauai Channel, Hawaii. *Eos, Trans. Amer. Geophys. Union,* **84,** OS39.

Leaman, K. D., and T. B. Sanford, 1975: Vertical energy propagation of internal waves: A vector spectral analysis of velocity profiles. *J. Geophys. Res.,* **80,** 1975–1978.

Ledwell, J. R., A. J. Watson, and C. S. Law, 1993: Evidence of slow mixing across the pycnocline from an open-ocean tracer-release experiment. *Nature,* **364,** 701–703.

——, E. T. Montgomery, K. L. Polzin, L. C. St. Laurent, R. W. Schmitt, and J. M. Toole, 2000: Evidence for enhanced mixing over rough topography in the abyssal ocean. *Nature,* **403,** 179–182.

Lien, R.-C., and M. C. Gregg, 2001: Observations of turbulence in a tidal beam and across a coastal ridge. *J. Geophys. Res.,* **106,** 4575–4591.

Lozovatsky, I. D., E. G. Morozov, and H. J. S. Fernando, 2003: Spatial decay of energy density of tidal internal waves. *J. Geophys. Res.,* **108,** 3201, doi:10.1029/2001JC001169.

Lueck, R. G., and T. D. Mudge, 1997: Topographically-induced mixing around a shallow seamount. *Science,* **276,** 1831–1833.

Lukas, R., F. Santiago-Mandujano, F. Bingham, and A. Mantyla, 2001: Cold bottom-water events observed in the Hawaii Ocean Time series: Implications for vertical mixing. *Deep-Sea Res.,* **48,** 995–1021.

Martin, J. P., D. L. Rudnick, and R. Pinkel, 2006: Spatially broad observations of internal waves in the upper ocean at the Hawaiian Ridge. *J. Phys. Oceanogr.,* **36,** 1085–1103.

Mauritzen, C., K. L. Polzin, M. S. McCartney, R. C. Millard, and D. E. West-Mack, 2002: Evidence in hydrography and density fine structure for enhanced vertical mixing over the Mid-Atlantic Ridge. *J. Geophys. Res.,* **107,** 3147, doi:10.1019/2001JC001114.

Merrifield, M. A., and P. E. Holloway, 2002: Model estimates of M_2 internal tide energetics at the Hawaiian Ridge. *J. Geophys. Res.,* **107,** 3179, doi:10.1029/2001JC000996.

——, ——, and T. S. Johnston, 2001: The generation of internal tides at the Hawaiian Ridge. *Geophys. Res. Lett.,* **28,** 559–562.

Morozov, E. G., 1995: Semidiurnal internal wave global field. *Deep-Sea Res.,* **42,** 135–148.

Moum, J. N., 1996: Energy-containing scales of turbulence in the ocean thermocline. *J. Geophys. Res.,* **101,** 14 095–14 109.

Munk, W., and C. Wunsch, 1998: Abyssal recipes II: Energetics of tidal and wind mixing. *Deep-Sea Res.,* **45,** 1977–2010.

Nabatov, V. N., and R. V. Ozmidov, 1988: Study of turbulence above seamounts in the Atlantic Ocean. *Oceanology,* **28,** 161–166.

Nash, J. D., E. Kunze, J. M. Toole, and R. W. Schmitt, 2004: Internal tide reflection and turbulent mixing on the continental slope. *J. Phys. Oceanogr.,* **34,** 1117–1134.

——, M. H. Alford, and E. Kunze, 2005: Estimating internal wave energy fluxes in the ocean. *J. Atmos. Oceanic Technol.,* **22,** 1551–1570.

——, E. Kunze, C. M. Lee, and T. B. Sanford, 2006: Structure of the baroclinic tide generated at Kaena Ridge, Hawaii. *J. Phys. Oceanogr.,* **36,** 1123–1135.

Nasmyth, P. W., 1970: Oceanic turbulence. Ph.D. thesis, University of British Columbia, 69 pp.

Niwa, Y., 1998: Numerical study of nonlinear energy transfer from large generation scale down to small dissipation scale across the oceanic internal-wave spectrum. Ph.D. thesis, Hokkaido University, 106 pp.

——, and T. Hibiya, 2001: Numerical study of the spatial distribution of the M_2 internal tide in the Pacific Ocean. *J. Geophys. Res.,* **106,** 22 441–22 449.

Oakey, N. S., 1982: Determination of the rate of dissipation of turbulent energy from simultaneous temperature and velocity shear microstructure measurements. *J. Phys. Oceanogr.,* **12,** 256–271.

Osborn, T. R., 1980: Estimates of the local rate of vertical diffusion from dissipation measurements. *J. Phys. Oceanogr.,* **10,** 83–89.

Pingree, R. D., and A. L. New, 1989: Downward propagation of internal tide energy into the Bay of Biscay. *Deep-Sea Res.,* **36,** 735–758.

——, and ——, 1991: Abyssal penetration and bottom reflection of internal tide energy in the Bay of Biscay. *J. Phys. Oceanogr.,* **21,** 28–39.

Pinkel, R., and Coauthors, 2000: Ocean mixing studied near Hawaiian Ridge. *Eos, Trans. Amer. Geophys. Union,* **81,** 545–553.

Rainville, L., and R. Pinkel, 2006: Propagation of low-mode internal waves through the ocean. *J. Phys. Oceanogr.,* **36,** 1220–1236.

Ray, R., and G. T. Mitchum, 1997: Surface manifestation of internal tides in the deep ocean: Observations from altimetry and island gauges. *Progress in Oceanography,* Vol. 40, Pergamon, 135–162.

——, and D. E. Cartwright, 2001: Estimates of internal tide energy-fluxes from TOPEX/Poseidon altimetry: Central North Pacific. *Geophys. Res. Lett.,* **28,** 1259–1262.

Rudnick, D. L., and Coauthors, 2003: From tides to mixing along the Hawaiian Ridge. *Science,* **301,** 355–357.

Sanford, T. B., R. G. Drever, and J. H. Dunlap, 1985: An acoustic Doppler and electromagnetic velocity profiler. *J. Atmos. Oceanic Technol.,* **2,** 1245–1257.

Simmons, H. L., R. W. Hallberg, and B. K. Arbic, 2004: Internal wave generation in a global baroclinic tide model. *Deep-Sea Res. II,* **51,** 3043–3068.

Sjöberg, B., and A. Stigebrandt, 1992: Computations of the geographical distribution of the energy-flux to mixing processes via internal tides and the associated vertical circulation in the ocean. *Deep-Sea Res.,* **39,** 269–291.

Smith, W. H. F., and D. T. Sandwell, 1997: Global seafloor topog-

raphy from satellite altimetry and ship depth soundings. *Science,* **277,** 1956–1962.

St. Laurent, L. S., and C. Garrett, 2002: The role of internal tides in mixing the deep ocean. *J. Phys. Oceanogr.,* **32,** 2882–2899.

——, S. Stringer, C. Garrett, and D. Perrault-Joncas, 2003: The generation of internal tides at abrupt topography. *Deep-Sea Res.,* **50,** 987–1003.

Toole, J. M., K. L. Polzin, and R. W. Schmitt, 1994: Estimates of diapycnal mixing in the abyssal ocean. *Science,* **264,** 1120–1123.

——, R. W. Schmitt, K. L. Polzin, and E. Kunze, 1997: Near-boundary mixing above the flanks of a midlatitude seamount. *J. Geophys. Res.,* **102,** 947–959.

Wesson, J. C., and M. C. Gregg, 1994: Mixing at Camarinal Sill in the Strait of Gibraltar. *J. Geophys. Res.,* **99,** 9847–9878.

Wunsch, C., 1975: Internal tides in the ocean. *Rev. Geophys. Space Phys.,* **13,** 167–182.